

Probing general relativistic spin-orbit coupling with gravitational waves from hierarchical triple systems

Marius A. Oancea,¹  Richard Stiskalek,^{2,3} and Miguel Zumalacárregui⁴

¹University of Vienna, Faculty of Physics, Boltzmannngasse 5, 1090 Vienna, Austria

²Astrophysics, University of Oxford, Denys Wilkinson Building, Keble Road, Oxford, OX1 3RH, UK

³Universitäts-Sternwarte, Ludwig-Maximilians-Universität München, Scheinerstr. 1, 81679 München, Germany

⁴Max Planck Institute for Gravitational Physics (Albert Einstein Institute), Am Mühlenberg 1, D-14476 Potsdam, Germany

September 24, 2024

ABSTRACT

Wave packets propagating in inhomogeneous media experience a coupling between internal and external degrees of freedom and, as a consequence, follow spin-dependent trajectories. These phenomena, well known in optics and condensed matter physics, are referred to as spin Hall effects. Similarly, the gravitational spin Hall effect is expected to affect the propagation of gravitational waves on curved spacetimes. In this general-relativistic setup, the curvature of spacetime acts as impurities in a semiconductor or inhomogeneities in an optical medium, leading to a frequency- and polarization-dependent propagation of wave packets. In this letter, we study this effect for strong-field lensed gravitational waves generated in hierarchical triple black hole systems in which a stellar-mass binary merges near a more massive black hole. We calculate how the gravitational spin Hall effect modifies the gravitational waveforms and show its potential for experimental observation. If detected, these effects will have profound implications for astrophysics and tests of general relativity.

Key words: gravitational waves – gravitational lensing: strong – polarization

1 INTRODUCTION

In optics and condensed matter physics, the dynamics of wave packets carrying intrinsic angular momentum can generally depend on spin-orbit interactions (Bliokh et al. 2015; Sinova et al. 2015; Manchon et al. 2015). This mechanism describes the mutual coupling between the external (average position and momentum) and internal (spin or polarization) degrees of freedom of the wave packet and is generally responsible for the spin Hall effects (Dyakonov & Khaetskii 2008; Sinova et al. 2015; Bliokh et al. 2015; Ling et al. 2017). These effects have been observed in several experiments (Bakun et al. 1984; Kato et al. 2004; Hosten & Kwiat 2008; Bliokh et al. 2008), and have led to a broad range of applications in spintronics, photonics, metrology, and optical communications (Jungwirth et al. 2012; Ling et al. 2017; Liu et al. 2022).

Similarly, spin-orbit interactions are also predicted to affect the dynamics of wave packets in gravitational fields through the gravitational spin Hall effect (GSHE), be it for electromagnetic (Oancea et al. 2020; Harte & Oancea 2022; Frolov 2020; Gosselin et al. 2007) or linearized gravitational (Andersson et al. 2021; Yamamoto 2018) waves propagating on curved spacetimes (see also Andersson & Oancea (2023); Oancea et al. (2019); Oancea & Kumar (2023); Li et al. (2022)). This implies a certain universality of spin Hall effects across different physical systems. The analogy that we can make between the general relativistic setup and other areas of physics is that black holes (BHs) in spacetime play a role similar to impurities in a semiconductor or inhomogeneities of an optical medium. Thus,

under the influence of gravity, wave packets carrying intrinsic angular momentum (as is the case with electromagnetic and gravitational waves) follow frequency- and polarization-dependent trajectories, reducing to geodesic motion only in the limit of infinite frequency, i.e. geometrical optics (GO). Given this frequency dependence, we expect gravitational waves (GWs) to represent the most favourable avenue for observing the GSHE.

GWs offer a precision probe of astrophysical phenomena (The LIGO Scientific Collaboration 2015; The LIGO Scientific Collaboration & the Virgo Collaboration 2016), carrying information on strong field dynamical gravity. Due to their low frequency, the GSHE is much less suppressed for GWs than for electromagnetic signals. A fraction of GW sources may merge in a high-curvature region. Active galactic nuclei (AGNs) or globular cluster binary formation channels (O’Leary et al. 2009; Martinez et al. 2020; Sedda et al. 2023; Stone et al. 2017; Secunda et al. 2019; Samsing et al. 2022; Gerosa & Fishbach 2021) provide environments where a GW source near another BH can produce a detectable GSHE signal. As the number of recorded GW events grows, so will the prospect of such a detection.

In this letter, we present compelling theoretical and numerical evidence for astrophysical configurations in which the GSHE is measurable on GW signals at the current detector sensitivity in optimal situations. We will discuss the GSHE, its imprint on waveforms, and the prospects for detection. Our results are mainly based on a numerical ray-tracing code for the GSHE, that we make publicly available at (Stiskalek et al. 2024). Further details about the numerical implementation, as well as other technical details can be found in (Oancea et al. 2024).

* E-mail: marius.oancea@univie.ac.at

2 GRAVITATIONAL SPIN HALL EFFECT

We investigate the lensing of GWs in hierarchical triple BH systems, where two stellar-mass BHs merge and emit GWs in the proximity of the third, much larger BH, which acts as a lens. We assume that the merging BHs are much smaller than the lens, so that we can use the following idealized model: the lens is represented by a fixed background Kerr BH, and the merging BHs are treated as a static point source of GWs. The emitted GWs are treated as small metric perturbations of the background Kerr BH, and are described by the linearized Einstein field equations.

In the GO approximation, the propagation of GWs is described by the null geodesics of the background spacetime (Misner et al. 1973, Sec. 35.13). However, this does not take into account the general relativistic spin-orbit coupling between the internal and external degrees of freedom of a wave packet. This appears as higher-order corrections to the GO approximation (Oancea et al. 2020; Andersson et al. 2021; Harte & Oancea 2022), resulting in frequency- and polarization-dependent wave packet propagation (GSHE). The equations of motion that describe the GSHE are (Andersson et al. 2021; Harte & Oancea 2022)

$$\dot{x}^\mu = p^\mu + \frac{1}{p \cdot t} S^{\mu\beta} p^\nu \nabla_\nu T_\beta, \quad (1a)$$

$$\dot{x}^\nu \nabla_\nu p_\mu = -\frac{1}{2} R_{\mu\nu\alpha\beta} p^\nu S^{\alpha\beta}. \quad (1b)$$

Here, external degrees of freedom are represented by $x^\mu(\tau)$, the worldline of the energy centroid of the wave packet, and the average wave packet momentum $p_\mu(\tau)$. The internal degree of freedom is represented by the spin tensor $S^{\alpha\beta}$, which encodes the angular momentum carried by the wave packet. The timelike vector field T^α is needed to fix the definition of the energy centroid of the wave packet (Harte & Oancea 2022) and can be related to the 4-velocities of the source and observer (Oancea et al. 2024), and $R_{\mu\nu\alpha\beta}$ is the Riemann tensor. Here, we consider circularly polarized wave packets, for which the spin tensor is uniquely fixed as

$$S^{\alpha\beta} = \frac{\epsilon s}{p \cdot T} \epsilon^{\alpha\beta\gamma\lambda} p_\gamma T_\lambda, \quad (2)$$

where $s = \pm 2$, depending on the state of circular polarization, ϵ is the Levi-Civita tensor and ϵ is a small dimensionless parameter used to keep track of the order of different terms in the high-frequency expansion leading to the above equations (Andersson et al. 2021; Harte & Oancea 2022); see also (Maggiore 2007, Sec. 1.5). The wave frequency f measured by an observer with 4-velocity T^α is defined as $p \cdot T = -\epsilon f$. For the hierarchical triple systems considered here, we define ϵ as the ratio of the wavelength λ of the GW (in the rest frame of the source) and half the Schwarzschild radius R_s of the background BH:

$$\epsilon = \frac{\lambda}{R_s/2} = \frac{c^2 \lambda}{GM}. \quad (3)$$

Since Eq. (1) is only valid for $\epsilon \ll 1$, we will always work in a regime where $\epsilon \leq 0.1$. In particular, the GSHE vanishes if $\epsilon \rightarrow 0$ and Eq. (1) reduce to the geodesic equations.

Equations (1) and (2) are a particular case of the Mathisson-Papapetrou equations, where \dot{x}^μ and p_μ are null, and the worldline is fixed by the Corinaldesi-Papapetrou spin supplementary condition $S_{\alpha\beta} T^\beta = 0$ (Harte & Oancea 2022). Furthermore, the spin-dependent correction terms in the equations can also be related to the components of a Berry curvature 2-form on phase space (Oancea et al. 2020; Andersson et al. 2021; Harte & Oancea 2022), as is also the case for spin Hall effects in condensed matter physics (Sundaram

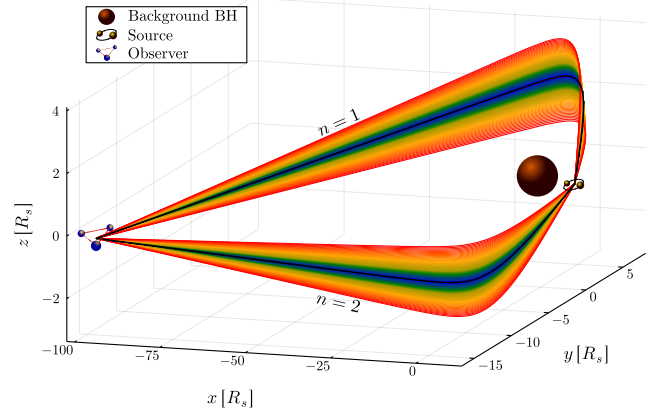


Figure 1. Two bundles of GSHE trajectories connecting a source at $(5 R_s, 0.5\pi, 0)$ to an observer at $(50 R_s, 0.4\pi, \pi)$. The background BH is Kerr with $a = 0.99M$. Each bundle consists of a null geodesic (black trajectory in the middle of the bundle, corresponding to $\epsilon s = 0$) and 100 GSHE rays with $s = \pm 2$ and $\epsilon \in [10^{-3}, 10^{-1.5}]$. The trajectories are coloured according to the value of ϵ , with red corresponding to longer wavelengths and violet corresponding to shorter wavelengths. Each bundle consists of two copies of a rainbow since for each finite wavelength there are two GSHE rays of opposite circular polarization ($s = \pm 2$).

& Niu 1999; Xiao et al. 2005; Sinova et al. 2015) and optics (Onoda et al. 2004; Bliokh et al. 2015).

We model the hierarchical triple BH system as a Kerr background BH of mass M and spin parameter a , together with a static point source of GWs placed close to the BH and a distant static observer. We use Eq. (1) to study the propagation of GWs between the source and the observer. The GSHE will be seen by the observer as a time delay between the frequency and polarization components of the waveform.

In Fig. 1, we show an example of two ϵs -parametrized bundles of trajectories that connect a source and an observer. Each bundle is centred along a null geodesic (corresponding to $\epsilon s = 0$), and we label different bundles with positive integers n , with $n = 1$ corresponding to the shortest path. Typically, there exist two distinct bundles of trajectories that directly connect a source and an observer, and several other bundles of trajectories that loop around the BH. We shall mainly focus on the directly connecting bundles and ignore the ones that loop around the BH, as the latter correspond to highly demagnified signals. The connecting trajectories are determined numerically, as outlined in (Oancea et al. 2024, Sec. II.C). This also yields the time of arrival of an ϵs -parametrized ray intersecting with the observer's worldline.

3 TIME DELAYS

The GSHE ray propagation induces a frequency- and polarization-dependent time of arrival. The observer proper time of arrival of rays in the n^{th} bundle is denoted by $\tau_{\text{GSHE}}^{(n)}(f, s)$, and we write the time delays as

$$\Delta\tau^{(n)}(\epsilon, s) = \tau_{\text{GSHE}}^{(n)}(\epsilon, s) - \tau_{\text{GO}}^{(n)}, \quad (4a)$$

$$\Delta\tau_{\text{R-L}}^{(n)}(\epsilon) = \tau_{\text{GSHE}}^{(n)}(\epsilon, s = +2) - \tau_{\text{GSHE}}^{(n)}(\epsilon, s = -2), \quad (4b)$$

where $\tau_{\text{GO}}^{(n)}$ is the geodesic proper time of arrival. The first equation is the dispersive GSHE-to-geodesic delay, and the second is the birefringent delay between the right- and left-polarized rays. We find that both the GSHE-to-geodesic and right-to-left delays can be well

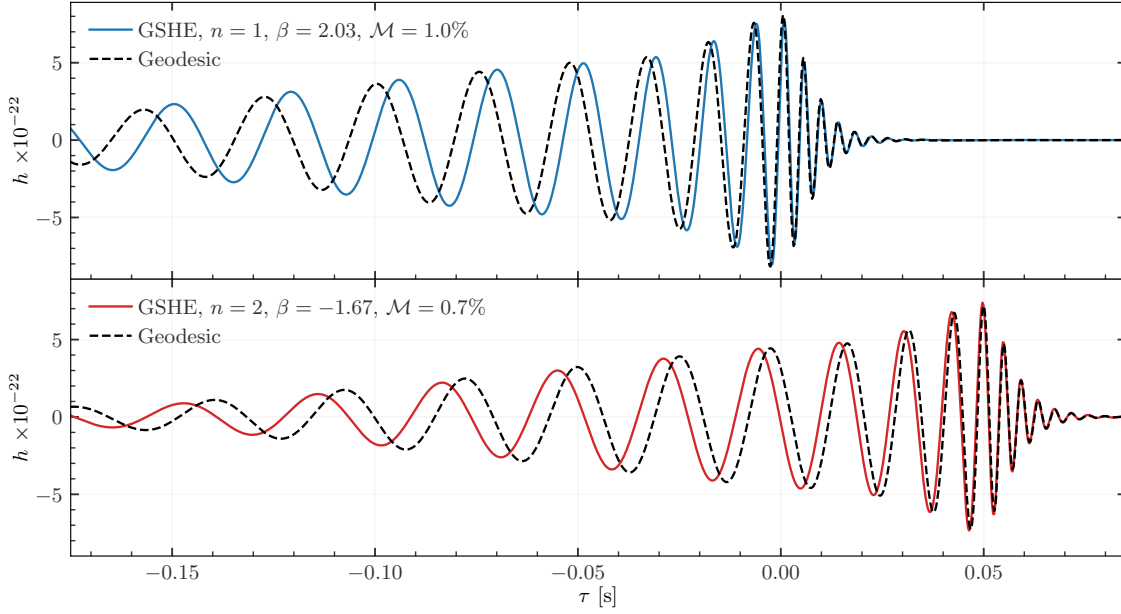


Figure 2. The waveform of a 50 and 35 M_{\odot} merger propagated along the two n -indexed bundles shown in Fig. 1 (top and bottom rows). The geodesic delay between bundles is $\tau_{\text{GO}}^{(2)} - \tau_{\text{GO}}^{(1)} = 50$ ms for this configuration. We assume $\lambda_{\text{max}}/R_s = 0.1$, where λ_{max} is the largest wavelength at 40 Hz, and report the mismatch \mathcal{M} . The GSHE is a frequency-dependent phase shift in the inspiral part of the signal.

approximated as a power law in frequency with proportionality factor β and exponent α as

$$\Delta\tau \approx \beta \sqrt{-g_{00}|x_{\text{obs}}|} \left(\frac{2c}{R_s} \frac{1}{f} \right)^{\alpha-1} \frac{1}{f}, \quad (5)$$

where $R_s = 2GM/c^2$ is the Schwarzschild radius of the background BH. For the GSHE-to-geodesic delay we denote the power law parameters by α, β and in the case of the birefringent delay by $\alpha_{\text{R-L}}, \beta_{\text{R-L}}$.

We find $\alpha \approx 2$ and $\alpha_{\text{R-L}} \approx 3$, independently of the configuration. On the other hand, the proportionality factors β and $\beta_{\text{R-L}}$ are determined by the mutual orientation of the source and the observer with respect to the background BH and its spin. The origin of the power law scaling and the dependence of the GSHE on the configuration are discussed in (Oancea et al. 2024, Sec. III.A). Note that $\beta_{\text{R-L}}$ is typically subdominant, but only zero in the Schwarzschild metric.

4 GRAVITATIONAL WAVEFORMS

The GSHE-induced time delay measured by the observer is frequency-dependent and weakly polarization-dependent. A gravitational waveform in a terrestrial detector typically spans a frequency range 2–1000 Hz (Buikema et al. 2020; Hild et al. 2011; Abbott et al. 2017; Reitze et al. 2019) and therefore its frequency components are delayed – either positively or negatively, depending on the sign of β – with respect to the original waveform emitted by the source. The frequency components of the unlensed waveform $\tilde{h}_0(f, s)$ are phase shifted so that in the circular polarization basis the GSHE-corrected waveform is

$$\tilde{h}_{\text{GSHE}}(f, s) = \sum_n e^{-2\pi i f \tau_{\text{GSHE}}^{(n)}(f, s)} \sqrt{|\mu^{(n)}(f, s)|} \tilde{h}_0(f, s). \quad (6)$$

The sum runs over the different images, that is, the bundles that connect the source and the observer. The magnification factor $\mu^{(n)}$ has a negligible dependence on f and s , so we will use its GO limit.

In Fig. 2, we show an example of the GSHE-induced frequency-dependent delay on an IMRPhenomXP (Pratten et al. 2021) waveform of a 50 and 35 M_{\odot} binary BH merger. The merger frequency is ~ 225 Hz, we set the lower frequency limit to 40 Hz and the background BH mass $M = 5 \times 10^4 M_{\odot}$. In this case, the maximum value of ϵ is 0.1, and the GSHE-to-geodesic delay is

$$\Delta\tau \approx 3 \text{ ms } \beta \left(\frac{5 \times 10^4 M_{\odot}}{M} \right) \left(\frac{40 \text{ Hz}}{f} \right)^2. \quad (7)$$

Due to the inverse quadratic scaling with frequency, the delay of the merger components is ~ 30 times less than that of the early inspiral at 40 Hz. The GSHE introduces a frequency-dependent phase shift in the inspiral part of the waveform, which is analogous to a non-zero graviton mass if $\beta > 0$ (Oancea et al. 2024, Sec. IV.E).

As a measure of distinguishability of the GSHE imprint on the waveform, we calculate the mismatch \mathcal{M} between \tilde{h}_{GSHE} and the corresponding GO signal (optimized over the coalescence phase and time), assuming a flat detector sensitivity (Oancea et al. 2024, Sec. II.E). In Fig. 2, for the configuration given in Fig. 1, we find that for the two bundles $\beta \approx 2$ and -1.7 and thus $\mathcal{M} \approx 1\%$. The GSHE is clearly distinguishable even for a moderate signal-to-noise ratio (SNR) (Lindblom et al. 2008). We further assess detectability using the equivalence of the GSHE (in the limit $\Delta\tau_{\text{L-R}} \sim 0$) to tests of the modified dispersion relation for GWs, as both predict a phase shift $\propto 1/f$ on the waveform. Posterior samples of the analysed LIGO-Virgo-Kagra (LVK) events (Abbott et al. 2019, 2021b,a) translate into $\sim \mathcal{O}(10^{-2})$ 90% c.l. limits on $|\beta|$, assuming $M = 5 \times 10^4 M_{\odot}$ (Oancea et al. 2024, Sec. II.D), in good agreement with the mismatch criterion. The comparison shows no strong degeneracies between GSHE and quasi-circular binary parameters. Additional effects can be included in \tilde{h}_0 (Eq. 6): Based on the different phase evolutions, we expect eccentricity (Tiwari et al. 2019) and environmental effects (Toubiana et al. 2021; Sberna et al. 2022) to be distinguishable from the GSHE. Microlensing by stellar fields can

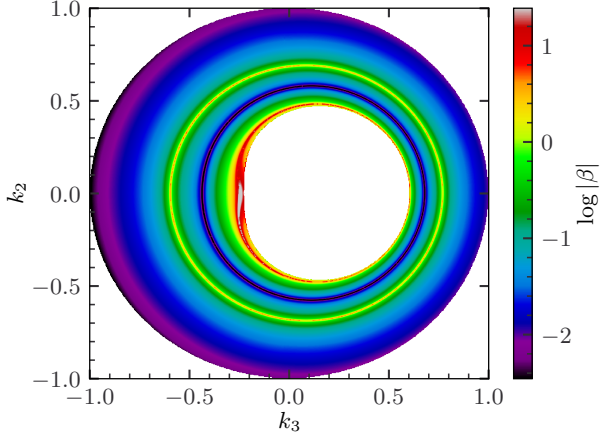


Figure 3. The GSHE-to-geodesic delay magnitude β as a function of the initial emission directions from the source computed with $\epsilon_{max} = 0.01$. These are parametrized by Cartesian coordinates k_2 and k_3 on the celestial sphere of the source, and the central white region represents the background BH shadow. The source is placed at $(5 R_s, \pi/2, 0)$ and the “observer” is defined as the point where the ϵ_{max} trajectory intersects the sphere of radius $50 R_s$. Each pixel represents an ϵ bundle of trajectories.

also be distinguished, as it causes stochastic variations on the phase and amplitude that oscillate in frequency (Diego et al. 2019; Mishra et al. 2021), in contrast to the monotonic frequency-dependent phase shift associated with the GSHE.

5 DETECTABILITY

Throughout this work, we have assumed a fiducial background BH mass of $5 \times 10^4 M_\odot$. In this regime, the wavelength of GWs detectable by terrestrial observatories is sufficiently large to deviate from the GO propagation without requiring a wave optics treatment (Tambalo et al. 2023; Leung et al. 2023) – the regime in which our GSHE calculation applies. We identify two favourable configurations that yield $|\beta| \geq 1$: aligned source and observer (Fig. 1) and non-aligned source-observer, where a strongly deflected trajectory grazes the shadow of the background BH. Both configurations are apparent in Fig. 3, where the dispersive GSHE amplitude is shown as a function of the emission direction for a source at $(5 R_s, \pi/2, 0)$. The outer ring of $|\beta| \geq 1$ corresponds to magnified bundles of trajectories toward observers closely aligned with the source-BH system. The inner region around the BH shadow boundary consists of bundles that are strongly deflected or even loop around the BH. These trajectories reach non-aligned observers but are highly demagnified.

We calculate that in the scenario of Fig. 3, approximately 5% of the initial directions on the celestial half-sphere of the source facing the BH yield $|\beta| \geq 0.5$, further scaling as the inverse square of the radial source distance from the background BH. Translating probabilities to the observer frame introduces a Jacobian element $|\mu|^{-1}$. This reflects how magnified images require a precise source-BH-observer alignment, while demagnified images are generic: there is at least one strongly deflected trajectory that grazes the light ring and reaches any observer. Trajectories with $|\mu| \ll 1$ and $|\beta| \geq 1$ are the main contributors to probability, even when demagnification is taken into account.

To estimate the detection probabilities, we define the effective

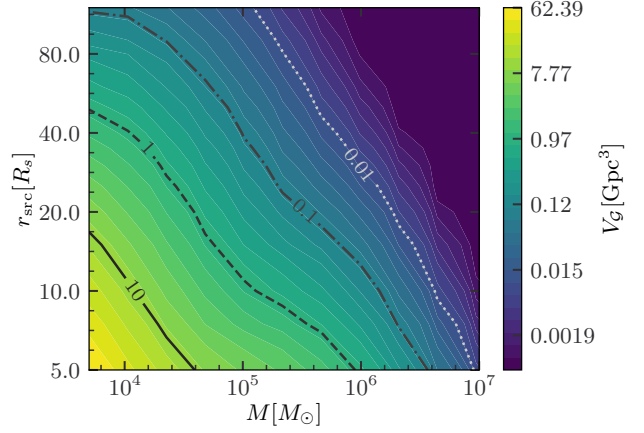


Figure 4. Effective volume for a $30 + 30 M_\odot$ non-spinning binary observed by Cosmic Explorer, as a function of the distance to the background BH and its mass.

GSHE observable volume

$$V_{\mathcal{G}} = \int dz \frac{dV_z}{dz}(z) \int d|\mu| P_{\text{det}} \frac{dY_{\text{obs}}}{d|\mu|}, \quad (8)$$

via an integral over source redshift and magnification of the product of comoving differential volume dV_z/dz , detected fraction P_{det} (Chen et al. 2021) and probability of observable GSHE in the observer sphere $dY_{\text{obs}}/d|\mu|$, both depending on the sources’ properties and SNR. Fig. 4 shows $V_{\mathcal{G}}$ for quasi-circular, non-spinning $30 + 30 M_\odot$ binary coalescences observed by Cosmic Explorer (Reitze et al. 2019) as a function of the mass of the background BH and its distance to the source (see (Oancea et al. 2024, Sec. IV.E) for details). The detection rate is $\dot{N}_{\text{obs}} \approx \mathcal{R} V_{\mathcal{G}}$, where the merger rate $\mathcal{R}(M, r_{\text{src}})$ is assumed to be constant.

Configurations where the GSHE is detectable may be realized in dense dynamical environments, such as globular and nuclear star clusters (O’Leary et al. 2009; Martinez et al. 2020; Sedda et al. 2023). These regions contain stellar-mass BHs and may also host intermediate-mass BHs: stellar-mass binaries may then merge close to a more massive object, either by chance (among the $\sim 10^5/\text{yr}$ mergers expected by future detectors) or because of its effects on the binary (e.g. if tidal interactions drive the merger as the binary approaches the intermediate-mass BH). In a favourable case, $r_{\text{src}} \sim 5 R_s$ and $M \sim 5 \times 10^4 M_\odot$, next-generation detectors reach an effective volume $\sim 30 \text{ Gpc}^3$. Another potential scenario consists of stellar-mass binary BHs in AGNs (Stone et al. 2017; Secunda et al. 2019; Samsing et al. 2022). There, BHs are expected to migrate inward due to interactions with the gas (Bellovary et al. 2016; Grishin et al. 2024) and become trapped close to the innermost stable circular orbit of the background BH (Peng & Chen 2021). In this case, the high mass of the background BH suppresses the amplitude in the frequency band of ground detectors. Nevertheless, Fig. 4 shows how Cosmic Explorer alone could detect GSHE in a binary near a $10^7 M_\odot$ BH at a characteristic distance $V_{\mathcal{G}}^{1/3} \sim 200 \text{ Mpc}$. Our estimate is conservative in this limit because our simulations do not resolve well the high β regime, which dominates the probabilities for large M .

The GSHE is a promising probe of the BH merger environment due to the frequency-dependent time delay. In addition, we expect to receive multiple, shortly spaced, images of the same merger along various bundles connecting the source and observer. The delay be-

tween the images and their relative magnification can be used to retrieve information about the BH mass and the orientation of the source-BH-observer system. The GSHE provides additional information, including a direct constraint on the spin of the background BH if the birefringence effect $\Delta\tau_{R-L}$ is observed. Moreover, neglecting the GSHE or the interference between multiple images can prevent detection, particularly for signals with low SNR (see Supplementary material).

6 CONCLUSIONS

We analysed the GSHE on the waveforms of lensed GWs. The GSHE is a strong field effect that describes the propagation of polarized wave packets. It produces a frequency-dependent delay in the inspiral part of the waveform, while keeping the merger and ringdown relatively unchanged, as shown in Fig. 2. The delay has a characteristic dispersive $1/f^2$ dependence, mimicking a non-zero graviton mass when $\beta > 0$ and may appear as a violation of Einstein's theory if not properly taken into account.

We identified two promising scenarios for the detection of the GSHE. One requires the source and observer to be aligned, leading to highly magnified images with a strong GSHE imprint. In this case, the source could be quite far from the background BH ($r_{\text{src}} \gg 5R_S$) and magnification bias facilitates the observation of the signal. In the second case the source and observer are not aligned and one of the bundles is strongly deflected, grazing the light ring of the background BH. These images are usually demagnified and too faint except for sources close to the background BH. AGNs and globular clusters, two of the formation channels for stellar-mass binary BHs, can potentially host such events. Although the number of such sources is unknown (Gerosa & Fishbach 2021), the GSHE provides additional means to investigate their existence.

In addition to coalescing stellar-mass binaries, the GSHE can also be detected for binaries in the early inspiral phase. This is a prime target for proposed low-frequency detectors in the μHz , mHz and dHz bands (Amaro-Seoane et al. 2017; Thorpe et al. 2019; Gong et al. 2021; Sedda et al. 2020; Baibhav et al. 2021; Sesana et al. 2021). The dependence of the corrections, Eq. (3), shows that low-frequency GW result in comparable signatures for much heavier background BHs, allowing the GSHE to probe central BHs of galaxies. Migration in these systems could plausibly drive stellar-mass objects towards very small radii (Peng & Chen 2021). The analysis of long-lived inspirals requires extending the framework to moving sources, a subject of future work. In addition, we expect the GSHE signal to be strongest when the GO expansion fails, $\epsilon \sim 1$. Exploring this regime requires a framework that combines wave optics and strong gravity (Cardoso et al. 2021; Pijenburg et al. 2024).

Detecting the GSHE can establish an association between stellar-mass binaries and more massive BHs. GSHE imprints due to intermediate-mass BHs provides new means to characterize these elusive objects, complementary to tidal disruption events (Wen et al. 2021), fast-moving stars in globular clusters (Häberle et al. 2024) and lensed gamma-ray bursts (Paynter et al. 2021; Yang et al. 2021; Wang et al. 2021). If observed in massive BHs, the GSHE will augment the knowledge of AGN binaries derived from their intrinsic parameters, peculiar motion or electromagnetic counterparts, and cross-correlation (Tagawa et al. 2020; Vijaykumar et al. 2023; Morton et al. 2023; Veronesi et al. 2023). This information will directly inform the binary formation scenarios and probe their close environment.

Furthermore, a detection of the GSHE will also confirm the

general-relativistic strong-field effects on the propagation of GWs, responsible for spin-orbit interactions of the same type as in optics (Bliokh et al. 2015) and condensed matter physics (Sinova et al. 2015). Discovering a GW source lensed by a BH will also provide an exquisite test of alternative gravity theories that produce modifications in regions of high curvature (Ezquiaga & Zumalacárregui 2020; Goyal et al. 2023; Eichhorn et al. 2023). Additionally, investigating the spacetime surrounding the background BH might be feasible, for instance, probing superradiant clouds due to ultralight bosons (Brito et al. 2020). In summary, GW observations offer potential for experimental verification of the GSHE, providing a test of GWs propagating in strong gravitational fields and potentially enabling novel applications in astrophysics and fundamental physics.

ACKNOWLEDGEMENTS

The authors thank Lars Andersson, Pedro Cunha, Dan D'Orazio, Francisco Duque, Héctor Estellés, Bence Kocsis, Johan Samsing, Laura Sberna and Jochen Weller for input and discussions, as well as the anonymous referee for constructive comments and recommendations. RS acknowledges financial support from STFC Grant No. ST/X508664/1 and the Deutscher Akademischer Austauschdienst (DAAD) Study Scholarship.

DATA AVAILABILITY

The code underlying this article is available at (Stiskalek et al. 2024) and other data will be made available on reasonable request to the authors.

SUPPLEMENTARY MATERIAL: GEOMETRICAL OPTICS & GRAVITATIONAL SPIN HALL EFFECT COMPLEMENTARITY

Here, we present some details of the complementarity between the GO and GSHE observations. To investigate the issue, we generated ~ 16000 pairs of trajectories connecting randomly placed sources and observers, assuming $r_{\text{src}} = 5R_S$ from a BH with spin $a = 0.99$.

Figure A1 shows the magnification $|\mu_i|$ and GSHE amplitude $|\beta_i|$. Positive/negative parity signals (trajectories 1/2) are marked in blue/red and color-coded by the time delay. A small fraction of the configurations has large $|\mu_i|$ and $|\beta_i|$, with a small time delay between the GO trajectories. This corresponds to a close alignment between the source, lens, and observer, similar to Figs. 1 and 2 in the main manuscript. Generic trajectories have a positive parity signal with $\mu_1 \sim 1$ (slightly below unity due to gravitational redshift) with a negative parity image with low amplitude $|\mu_2| \ll 1$ and a sizeable GSHE β_2 .

The detectability of multiple GO images and GSHE signatures depends mainly on the unlensed SNR (ρ_0). We want to distinguish whether a signal is *detectable* (with optimal analysis) and *detected* (using standard techniques). We assume that a GO signal is detected if

$$\sqrt{|\mu_i|} (1 - \mathcal{M}(\beta_i)) \rho_0 \geq \rho_{\text{th}} \quad (\text{GO detected}), \quad (\text{A1})$$

where $\rho_{\text{th}} = 8$ is the detection threshold and $\mathcal{M}(\beta_i)$ is the mismatch due to the GSHE (Oancea et al. 2024, Sec. II.E), which can prevent the identification of a signal. In contrast, a signal is detectable for

$$\sqrt{|\mu_i|} \rho_0 \geq \rho_{\text{th}} \quad (\text{GO detectable}), \quad (\text{A2})$$

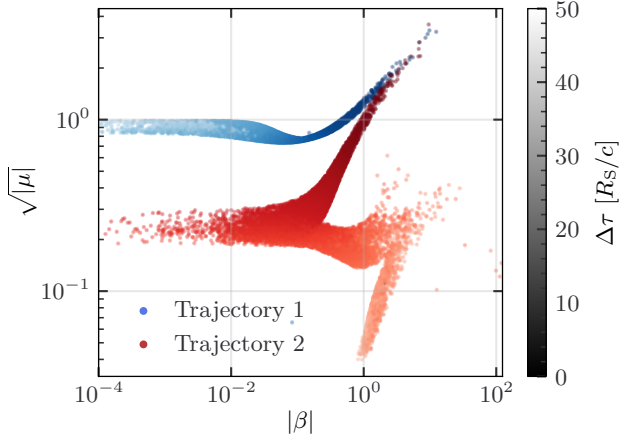


Figure A1. GO signal and GSHE amplitude for images 1 & 2 (blue/red), for $r_{\text{src}} = 5 R_s$, $a = 0.99$. Points are color coded by the time delay between GO images, with darker values corresponding to closer arrival times.

if the GSHE is accounted for. We will consider the GSHE detected/detectable if $\sqrt{|\mu_i|} \mathcal{M}(\beta_i) \rho_0 > 1$ (Oancea et al. 2024, Sec. IV.E), in addition to Eqs. (A1) and (A2). For concreteness, we will now assume a lens BH with $M = 10^4 M_\odot$ and a non-spinning equal mass source with total mass $20 M_\odot$.

Figure A2 shows the fraction of signals that satisfy the following conditions as a function of the unlensed SNR:

- (i) GO signal is detected (dotted)
- (ii) GO & GSHE are detectable (solid)
- (iii) GO missed due to GSHE (dashed dotted).
- (iv) GSHE is detectable in signal 1, but signal 2 below threshold (dashed)

For large $\rho_0 \gtrsim 50$ both GO signals are almost always detected, along with the GSHE imprints in most cases. The risk of missing a GO image by not accounting for the GSHE is low for the negative-parity image ($\lesssim 5\%$) and negligible for the positive-parity image. The high ρ_0 situation is expected for next-generation detectors, which are not magnitude limited.

The GSHE plays a crucial role for sources near or below the detection threshold $\rho_0 \lesssim \rho_{\text{th}}$. The fraction of missed signals can be substantial $\sim 80\%$, as detectable signals represent aligned configurations with high $|\mu_i|$ and $|\beta_i|$ (top right of Fig. A1). There is also a significant chance (20 – 80%) that a BH near the source can only be detected by measuring $\beta_1 \neq 0$ on the positive-parity image, since image 2 is undetectable even when accounting for GSHE (Fig. A2 bottom, dashed line). This probability is significant even for moderate SNR $\rho_0 \lesssim 20$. Incorporating the GSHE in the analysis can therefore be important at the current detector sensitivity, where most detected sources have SNR close to the detection threshold, and magnification bias may play an important role.

Our analysis has neglected both birefringent GSHE (β_{LR}) and the fact that multiple families of trajectories can interfere if the time delay is short. Both of these factors increase the mismatch, which reinforces the need for more detailed modeling to test the GSHE. The impact of β_{LR} is suppressed by an additional power of $1/f$. However, a fraction of the trajectories have $|\beta_{LR}| \gg |\beta|$. Ultimately, the impact of birefringent GSHE on the waveform depends on the

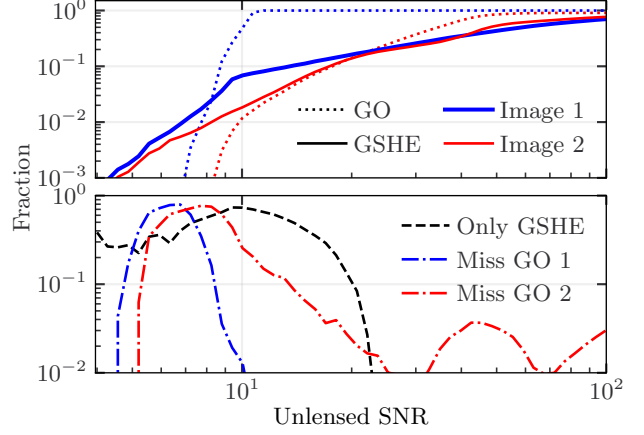


Figure A2. GO & GSHE complementarity. **Top:** fraction of signals with a detection of GO (dotted) and potentially detectable GSHE (solid) for $\rho_{\text{th}} = 8$, binary total mass $20 M_\odot$, lens BH with $M = 10^4 M_\odot$ and source at $5 R_s$. **Bottom:** Fraction of signals where a BH is detectable via GSHE (dashed) and where a GO image is missed due to GSHE (dot-dashed).

GW polarization (i.e. via the inclination angle): we will leave a quantitative analysis for a future study.

The probability of overlapping signals depends on the time delay distribution. This is shown in Fig. A3 for the system considered in the main part of the paper ($M = 5 \cdot 10^4 M_\odot$, $a = 0.99$, $r_{\text{src}} = 5 R_s$), for arbitrary trajectories and those with comparable amplitudes $|\mu_2/\mu_1| > 0.5$. Overlapping trajectories are generally a small fraction ($\lesssim 0.4\%$ with $\Delta\tau < 0.3\text{s}$), but become more likely when GO signals have a comparable amplitude ($\lesssim 10\%$ with $\Delta\tau < 0.3\text{s}$ and $|\mu_2/\mu_1| > 0.5$). Accounting for interference will be important to detect and analyze aligned source-BH-lens configurations, where both magnifications and GSHE are large (e.g. Figs. 1 and 2 in the letter).

We also assumed that the same detection threshold holds for both GO signals. However, once the brighter signal has been identified, a dedicated analysis can find an image with a lower ρ_{th} (Wang & Nitz 2022) (with or without accounting for GSHE). Other factors, such as source motion (Zhang & Chen 2023) and orbital inclination (Gondán & Kocsis 2022) cause differences between GO signals and need to be taken into account. Our analysis has assumed a source close to an intermediate mass BH ($M = 10^4 M_\odot$, $r_{\text{src}} = 5 R_s$). Higher/lower BH masses will make the GSHE less/more relevant (although lighter lenses will require a wave-optics treatment of strong fields, currently not available). Increasing the source’s distance lowers the magnification of strongly deflected trajectories, reducing the detectability of generic configurations. However, the GSHE remains important for close source-BH-observer alignments, which will happen in a fraction of sources $\propto R_s/r_{\text{src}}$. Given the growing rate of GW detections, the GSHE opens a new avenue for studying intermediate mass BHs and their properties.

References

- Abbott B. P., et al., 2017, *Classical and Quantum Gravity*, 34, 044001
- Abbott B. P., et al., 2019, *Physical Review D*, 100, 104036
- Abbott R., et al., 2021a, arXiv:2112.06861
- Abbott R., et al., 2021b, *Physical Review D*, 103, 122002
- Amaro-Seoane P., et al., 2017, arXiv:1702.00786

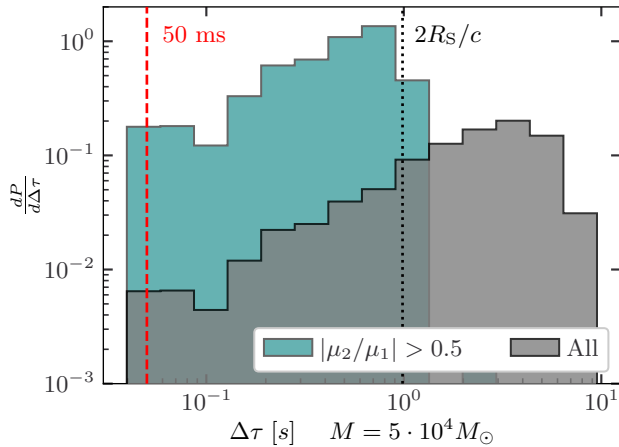


Figure A3. Distribution of the time delays between GO trajectories. Two cases are shown: all trajectories (gray) and those where both GO signals have comparable amplitude (teal): this selects closer source-lens-observer alignments, for which the time delay is smaller. The vertical lines show the time delay in Figs. 1 and 2 of the letter and the characteristic scale.

Andersson L., Oancea M. A., 2023, *Classical and Quantum Gravity*, 40, 154002

Andersson L., Joudioux J., Oancea M. A., Raj A., 2021, *Physical Review D*, 103, 044053

Baibhav V., et al., 2021, *Experimental Astronomy*, 51, 1385

Bakun A. A., Zakharchenya B. P., Rogachev A. A., Tkachuk M. N., Fleisher V. G., 1984, *Soviet Journal of Experimental and Theoretical Physics Letters*, 40, 1293

Bellovary J. M., Mac Low M.-M., McKernan B., Ford K. E. S., 2016, *The Astrophysical Journal Letters*, 819, L17

Bliokh K. Y., Niv A., Kleiner V., Hasman E., 2008, *Nature Photonics*, 2, 748

Bliokh K. Y., Rodríguez-Fortuño F. J., Nori F., Zayats A. V., 2015, *Nature Photonics*, 9, 796

Brito R., Cardoso V., Pani P., 2020, *Superradiance: New Frontiers in Black Hole Physics*. LNP 971, Springer Cham, doi:10.1007/978-3-319-19000-6

Buikema A., et al., 2020, *Physical Review D*, 102, 062003

Cardoso V., Duque F., Khanna G., 2021, *Physical Review D*, 103, L081501

Chen H.-Y., Holz D. E., Miller J., Evans M., Vitale S., Creighton J., 2021, *Classical Quantum Gravity*, 38, 055010

Diego J. M., Hannuksela O. A., Kelly P. L., Broadhurst T., Kim K., Li T. G. F., Smoot G. F., Pagano G., 2019, *Astronomy & Astrophysics*, 627, A130

Dyakonov M. I., Khaetskii A. V., 2008, *Spin Hall Effect*. Springer Berlin Heidelberg, pp 211–243, doi:10.1007/978-3-540-78820-1_8

Eichhorn A., Fernandes P. G. S., Held A., Silva H. O., 2023, arXiv:2312.11430

Ezquiaga J. M., Zumalacárregui M., 2020, *Physical Review D*, 102, 124048

Frolov V. P., 2020, *Physical Review D*, 102, 084013

Gerosa D., Fishbach M., 2021, *Nature Astronomy*, 5, 749

Gondán L., Kocsis B., 2022, *Monthly Notices of the Royal Astronomical Society*, 515, 3299

Gong Y., Luo J., Wang B., 2021, *Nature Astronomy*, 5, 881

Gosselin P., Bérard A., Mohrbach H., 2007, *Physical Review D*, 75, 084035

Goyal S., Vijaykumar A., Ezquiaga J. M., Zumalacárregui M., 2023, *Physical Review D*, 108, 024052

Grishin E., Gilbaum S., Stone N. C., 2024, *Monthly Notices of the Royal Astronomical Society*, 530, 2114

Häberle M., et al., 2024, *Nature*, 631, 285

Harte A. I., Oancea M. A., 2022, *Physical Review D*, 105, 104061

Hild S., et al., 2011, *Classical and Quantum Gravity*, 28, 094013

Hosten O., Kwiat P., 2008, *Science*, 319, 787

Jungwirth T., Wunderlich J., Olejník K., 2012, *Nature Materials*, 11, 382

Kato Y. K., Myers R. C., Gossard A. C., Awaschalom D. D., 2004, *Science*, 306, 1910

Leung C., Jow D., Saha P., Dai L., Oguri M., Koopmans L. V. E., 2023, arXiv:2304.01202

Li Z., Qiao J., Zhao W., Er X., 2022, *Journal of Cosmology and Astroparticle Physics*, 2022, 095

Lindblom L., Owen B. J., Brown D. A., 2008, *Physical Review D*, 78, 124020

Ling X., Zhou X., Huang K., Liu Y., Qiu C.-W., Luo H., Wen S., 2017, *Reports on Progress in Physics*, 80, 066401

Liu S., Chen S., Wen S., Luo H., 2022, *Opto-Electronic Science*, 1, 220007

Maggiore M., 2007, *Gravitational Waves: Volume 1: Theory and Experiments*. Oxford University Press, doi:10.1093/acprof:oso/9780198570745.001.0001

Manchon A., Koo H. C., Nitta J., Frolov S. M., Duine R. A., 2015, *Nature Materials*, 14, 871

Martinez M. A. S., et al., 2020, *The Astrophysical Journal*, 903, 67

Mishra A., Meena A. K., More A., Bose S., Bagla J. S., 2021, *Monthly Notices of the Royal Astronomical Society*, 508, 4869

Misner C. W., Thorne K. S., Wheeler J. A., 1973, *Gravitation*. W. H. Freeman San Francisco

Morton S. L., Rinaldi S., Torres-Orjuela A., Derdzinski A., Vaccaro M. P., Del Pozzo W., 2023, *Physical Review D*, 108, 123039

O’Leary R. M., Kocsis B., Loeb A., 2009, *Monthly Notices of the Royal Astronomical Society*, 395, 2127

Oancea M. A., Kumar A., 2023, *Physical Review D*, 107, 044029

Oancea M. A., Paganini C. F., Joudioux J., Andersson L., 2019, arXiv:1904.09963

Oancea M. A., Joudioux J., Dodin I. Y., Ruiz D. E., Paganini C. F., Andersson L., 2020, *Physical Review D*, 102, 024075

Oancea M. A., Stiskalek R., Zumalacárregui M., 2024, *Physical Review D*, 109, 124045

Onoda M., Murakami S., Nagaosa N., 2004, *Physical Review Letters*, 93, 083901

Paynter J., Webster R., Thrane E., 2021, *Nature Astronomy*, 5, 560

Peng P., Chen X., 2021, *Monthly Notices of the Royal Astronomical Society*, 505, 1324

Pijenburg M., Cusin G., Pitrou C., Uzan J.-P., 2024, arXiv:2404.07186

Pratten G., et al., 2021, *Physical Review D*, 103, 104056

Reitze D., et al., 2019, *Bulletin of the American Astronomical Society*, 51, 035

Samsing J., et al., 2022, *Nature*, 603, 237

Sberna L., et al., 2022, *Physical Review D*, 106, 064056

Secunda A., Bellovary J., Mac Low M.-M., Saavik Ford K. E., McKernan B., Leigh N., Lyra W., Sándor Z., 2019, *The Astrophysical Journal*, 878, 85

Sedda M. A., et al., 2020, *Classical and Quantum Gravity*, 37, 215011

Sedda M. A., Naoz S., Kocsis B., 2023, *Universe*, 9, 138

Sesana A., et al., 2021, *Experimental Astronomy*, 51, 1333

Sinova J., Valenzuela S. O., Wunderlich J., Back C. H., Jungwirth T., 2015, *Reviews of Modern Physics*, 87, 1213

Stiskalek R., Zumalacárregui M., Oancea M. A., 2024, Numerical implementation of the gravitational spin Hall effect, doi:10.5281/zenodo.13735932

Stone N. C., Metzger B. D., Haiman Z., 2017, *Monthly Notices of the Royal Astronomical Society*, 464, 946

Sundaram G., Niu Q., 1999, *Physical Review B*, 59, 14915

Tagawa H., Haiman Z., Kocsis B., 2020, *The Astrophysical Journal*, 898, 25

Tambalo G., Zumalacárregui M., Dai L., Cheung M. H.-Y., 2023, *Physical Review D*, 108, 043527

The LIGO Scientific Collaboration 2015, *Classical and Quantum Gravity*, 32, 074001

The LIGO Scientific Collaboration the Virgo Collaboration 2016, *Physical Review Letters*, 116, 061102

Thorpe J. I., et al., 2019, *Bulletin of the AAS*, 51

Tiwari S., Achamveedu G., Haney M., Hemantakumar P., 2019, *Physical Review D*, 99, 124008

Toubiana A., et al., 2021, *Physical Review Letters*, 126, 101105

Veronesi N., Rossi E. M., van Velzen S., 2023, *Monthly Notices of the Royal Astronomical Society*, 526, 6031

- Vijaykumar A., Tiwari A., Kapadia S. J., Arun K. G., Ajith P., 2023, [The Astrophysical Journal](#), 954, 105
- Wang Y.-F., Nitz A. H., 2022, [The Astrophysical Journal](#), 937, 89
- Wang Y., Jiang L.-Y., Li C.-K., Ren J., Tang S.-P., Zhou Z.-M., Liang Y.-F., Fan Y.-Z., 2021, [The Astrophysical Journal Letters](#), 918, L34
- Wen S., Jonker P. G., Stone N. C., Zabludoff A. I., 2021, [The Astrophysical Journal](#), 918, 46
- Xiao D., Shi J., Niu Q., 2005, [Physical Review Letters](#), 95, 137204
- Yamamoto N., 2018, [Physical Review D](#), 98, 061701
- Yang X., Lü H.-J., Yuan H.-Y., Rice J., Zhang Z., Zhang B.-B., Liang E.-W., 2021, [The Astrophysical Journal Letters](#), 921, L29
- Zhang X., Chen X., 2023, [Monthly Notices of the Royal Astronomical Society](#), 521, 2919

This paper has been typeset from a \TeX/L\AA\TeX file prepared by the author.